Geophysical Research Letters

RESEARCH LETTER
10.1029/2020GL087311

Key Points:
- Our extended database of whistler mode chorus allows us to probe the near-equatorial region in great detail, revealing new features
- In the equatorial generation region strong chorus is most extensive in the 0.1–0.4f_{ce} bands in the region 21–11 MLT from $L^* = 4$–8 and beyond
- At higher latitudes ($12 < |\lambda_m| < 18°$) strong chorus is largely restricted to the 0.1–0.3f_{ce} bands in the prenoon sector, from $L^* = 6$ to 8

Correspondence to:
N. P. Meredith,
nmer@bas.ac.uk

Citation:
Meredith, N. P., Horne, R. B., Shen, X.-C., Li, W., & Bortnik, J. (2020). Global model of whistler mode chorus in the near-equatorial region ($|\lambda_m| < 18°$). *Geophysical Research Letters*, *47*, e2020GL087311. https://doi.org/10.1029/2020GL087311

Received 30 JAN 2020
Accepted 6 MAY 2020
Accepted article online 24 MAY 2020

Global Model of Whistler Mode Chorus in the Near-Equatorial Region ($|\lambda_m| < 18°$)

Nigel P. Meredith[1], **Richard B. Horne**[1], **Xiao-Chen Shen**[2], **Wen Li**[2], **and Jacob Bortnik**[3]

[1]Natural Environment Research Council, British Antarctic Survey, Cambridge, UK , [2]Centre for Space Physics, Boston University, Boston, MA, USA , [3]Department of Atmospheric and Oceanic Sciences, University of California, Los Angeles, CA, USA

Abstract We extend our database of whistler mode chorus, based on data from seven satellites, by including ~3 years of data from Radiation Belt Storm Probes (RBSP)-A and RBSP-B and an additional ~6 years of data from Time History of Events and Macroscale Interactions during Substorms (THEMIS)-A, THEMIS-D, and THEMIS-E. The new database allows us to probe the near-equatorial region in detail, revealing new features. In the equatorial source region, $|\lambda_m| < 6°$, strong wave power is most extensive in the 0.1–0.4f_{ce} bands in the region 21–11 magnetic local time (MLT) from the plasmapause out to $L^* = 8$ and beyond, especially near dawn. At higher frequencies, in the 0.4–0.6f_{ce} frequency bands, strong wave power is more tightly confined, typically being restricted to the postmidnight sector in the region $4< L^* <6$. The global distribution of strong chorus wave power changes dramatically with increasing magnetic latitude, with strong chorus waves in the region $12< |\lambda_m| < 18°$ predominantly observed at frequencies below 0.3f_{ce} in the prenoon sector, in the region $5< L^* <8$.

1. Introduction

Chorus emissions are intense, naturally occurring, right-hand polarized, electromagnetic waves that propagate in the whistler mode. They typically occur in short, ~0.1 s, relatively coherent and repetitive bursts, with rising or, less often, falling tones, at frequencies below the local electron gyrofrequency, f_{ce} (e.g., Li et al., 2012; Santolík et al., 2004). The waves are generated outside the plasmapause near the geomagnetic equator (Lauben et al., 2002; LeDocq et al., 1998) by anisotropic distributions of energetic electrons with energies in the range of approximately keV to ~100 keV (e.g., Li et al., 2010; Omura et al., 2008) injected into the inner magnetosphere during storms and substorms. Consequently, chorus is observed largely outside the plasmapause and is substorm dependent with the largest intensities being seen during active conditions (Agapitov et al., 2018; Li et al., 2009; Meredith et al., 2001; Miyoshi et al., 2013). The waves often have a power gap at 0.5f_{ce}, which separates the emissions into so called lower-band ($0.1f_{ce} < f < 0.5f_{ce}$) and upper-band ($0.5f_{ce} < f < f_{ce}$) chorus (Koons & Roeder, 1990; Tsurutani & Smith, 1977). The cause of the gap remains an open question in magnetospheric physics and is particularly challenging since the gap is not an omnipresent feature (Teng et al., 2019) and, when present, varies in central frequency and bandwidth (Gao et al., 2019).

Chorus is an important magnetospheric emission due to its fundamental roles in radiation belt dynamics and in the production of the diffuse and pulsating aurora. For example, chorus is largely responsible for the acceleration of electrons to relativistic energies in the Earth's outer radiation belt that typically occurs during the recovery phase of geoeffective storms (e.g., Horne et al., 2005; Thorne, 2013; Tu et al., 2014). In contrast, storm time chorus at high latitudes causes microburst precipitation and may lead to losses of radiation belt electrons on the time scale of the order of a day (Lorentzen et al., 2001; Miyoshi et al., 2015; Thorne et al., 2005). Chorus has also been proposed as a source of plasmaspheric hiss (Bortnik et al., 2008; Bortnik et al., 2009), which is itself responsible for the formation of the slot region between the inner and outer radiation belt (Lyons & Thorne, 1973; Meredith et al., 2007, 2009), but its overall contribution to the observed magnetic local time (MLT) distribution of plasmaspheric hiss wave power is still a topic of debate (Hartley et al., 2019). At lower electron energies, pitch angle scattering by whistler mode chorus is largely responsible for both the diffuse aurora (Thorne et al., 2010) and the pulsating aurora (Nishimura et al., 2010).

Accurate models of whistler mode chorus are essential for radiation belt models. In this study we extend our existing database of whistler mode chorus (Meredith et al., 2012) by including ~3 years of data from Van

Allen Probes, Radiation Belt Storm Probes (RBSP)-A and RBSP-B, and an additional ~6 years of data from each of Time History of Events and Macroscale Interactions during Substorms (THEMIS)-A, THEMIS-D, and THEMIS-E spacecraft, greatly improving the statistics and coverage in the near-equatorial region ($|\lambda_m| < 18°$). The improved statistics allows us to study the global distribution of the emissions at a higher spatial resolution and to clearly separate generation from propagation effects in the global distribution of the chorus waves as a function of position and normalized frequency. The satellites, associated instrumentation, and data analysis techniques used to develop the model are briefly described in section 2. The global morphology of chorus as a function of spatial location and normalized frequency is then presented in section 3. Finally, the results are discussed and the conclusions are presented in sections 4 and 5, respectively.

2. Instrumentation and Data Analysis

To construct a comprehensive database of near-equatorial chorus in the inner magnetosphere, we combined data from seven satellites. We used 2.8 years of data from Dynamics Explorer 1, 1 year of data from Double Star TC1, 7.8 years of data from THEMIS-A, THEMIS-D, and THEMIS-E, and 2.8 years of data from RBSP-A and RBSP-B. Compared to the original database (Meredith et al., 2012), we exclude the wave measurements from CRRES and Cluster 1 so that we do not require a potentially inaccurate conversion from wave electric to magnetic field and also omit any electrostatic wave power in the chorus band. Details of the methods used to analyze the wave data from DE1, Double Star TC1, and THEMIS-A, THEMIS-D, and THEMIS-E are given in Meredith et al. (2012), and those used to analyze the RBSP-A and RBSP-B wave data are given in Li et al. (2015). Chorus waves can overlap in frequency with plasmaspheric emissions such as plasmaspheric hiss and lightning generated whistlers. We excluded these latter emissions from our study by adopting geomagnetic activity dependent templates to separate chorus from plasmaspheric emissions as described in Meredith et al. (2018).

We binned the chorus wave power from each satellite in nine normalized frequency bands between $0.1f_{ce}$ and $0.9f_{ce}$ as a function of L^*, MLT, magnetic latitude (λ_m), and geomagnetic activity as monitored by the *AE* index as detailed in Table 2 in Meredith et al. (2012). For the database L^* and MLT were computed using the Olson-Pfitzer quiet time model (Olson & Pfitzer, 1977) and the International Geomagnetic Reference Field (IGRF) at the middle of the appropriate year. Since the software is designed for particles and we are using it for waves, we assume a local pitch angle of 90° in the calculation of L^*. We then combined the data from each of the satellites, weighting the data from each individual satellite by the corresponding number of samples, to produce a combined wave database as a function of normalized frequency, L^*, MLT, λ_m, and geomagnetic activity.

Addition of the new wave data significantly improves the statistics and coverage in the near-equatorial region. For example, the average number of samples of lower-band chorus per L^*, MLT bin in the region $|\lambda_m| < 15°$ for $5 < L^* < 10$ during active conditions, $300 < AE < 1{,}000$ nT, with and without the new wave data is 9,847 and 94, respectively, increasing the average number of samples in each L^*, MLT bin by a factor of greater than 100. The improved database enables us to examine the global distribution of the wave power in the near-equatorial region at a latitudinal resolution of 6°, compared with 10° in Li et al. (2009) and 15° in Meredith et al. (2012), revealing new features.

3. Global Morphology

3.1. Global Distribution of Lower and Upper-Band Chorus in the Equatorial Region

Figure 1 presents the global distribution of the average wave intensity of lower-band chorus (bottom panels) and upper-band chorus (top panels) in the equatorial region ($|\lambda_m| < 6°$) as a function of L^* and MLT, for, from left to right, increasing geomagnetic activity as monitored by the *AE* index. Each plot extends linearly out to $L^* = 10$ with noon at the top and dawn to the right. The average intensities are shown in the large panels, and the corresponding sampling distributions in the small panels. Both the lower- and upper-band chorus are substorm dependent, with the strongest wave power being observed during active conditions, as found in previous studies. The region of strong lower-band chorus wave power extends from about 21 MLT through dawn to noon. The lower-band chorus is most extensive in L^* around dawn, ranging from $L^* = 4$ to 10. The upper-band chorus is also substorm dependent but much weaker. The upper-band chorus power is strongest during active conditions over a similar range of local times but is not as extensive as the lower-band chorus, tending to be confined to the region $4 < L^* < 7$. However, the frequency bands of lower- and upper-band

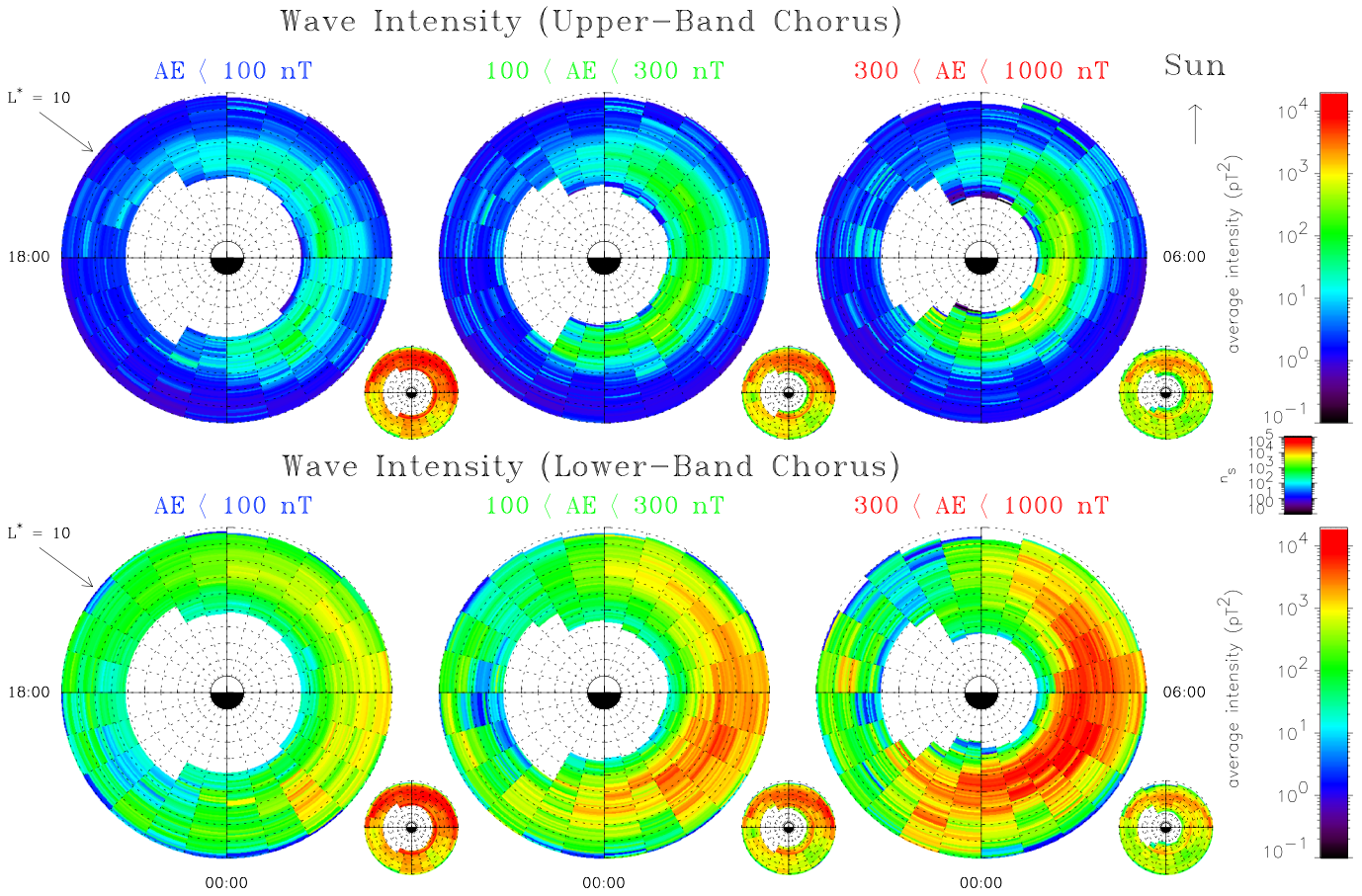

Figure 1. Global maps of the average wave intensity of lower- and upper-band chorus in the equatorial region, $|\lambda_m| < 6°$, as a function of L^* and MLT for three geomagnetic activity levels as monitored by the *AE* index. The maps extend linearly out to $L^* = 10$ with noon at the top and dawn to the right. The average intensities are shown in the large panels, and the corresponding sampling distributions in the small panels.

chorus are quite broad, masking any frequency dependence within each respective band. In the next section we investigate the spatial and frequency dependence of the chorus waves in detail.

3.2. MLT Distribution

To investigate the spatial and frequency dependence of lower-band chorus we plot the average wave intensity during active conditions, when the strongest waves are observed, as a function of L^* and MLT in Figure 2, for, from bottom to top, increasing frequency and, from left to right, increasing magnetic latitude. Strong waves, which we define as those with intensities greater than 500 pT^2, are observed in the equatorial region, $|\lambda_m| < 6°$, in each of the four normalized frequency bands (left panels). However, the spatial extent of the strong waves is frequency dependent. Strong waves cover the largest region of geospace in the 0.2–0.3f_{ce} band (Figure 2g). Here they are observed predominantly in the region 21 MLT through dawn to 11 MLT. The radial extent of the strongest waves is MLT dependent, being typically observed in the range $4.5 < L^* < 8$ near midnight, $5 < L^* < 10$ near dawn and $6 < L^* < 9$ near 09 MLT. The spatial extent of the strong waves is not quite as large in the 0.1–0.2f_{ce} (Figure 2j) and 0.3–0.4f_{ce} (Figure 2d) bands compared to the 0.2–0.3f_{ce} band (Figure 2g). However, in the highest frequency band, 0.4–0.5f_{ce}, the region of strong wave power is much reduced, typically being confined to the postmidnight sector for $4 < L^* < 6$ (Figure 2a).

The spatial distribution of the wave power changes dramatically with increasing magnetic latitude. Moving away from the equator, in the region $6 < |\lambda_m| < 12°$, strong waves are observed in the frequency bands between 0.1 and 0.4f_{ce}. Strong waves in this region cover the largest region of geospace in the 0.2–0.3f_{ce} band. On the dayside the spatial extent of the strong waves (Figure 2h) is similar to that observed in the equatorial region (Figure 2g). However, on the nightside the spatial extent of the strong waves is much smaller (Figure 2h), typically being confined to the region $4 < L^* < 6$ in the postmidnight sector. In particular,

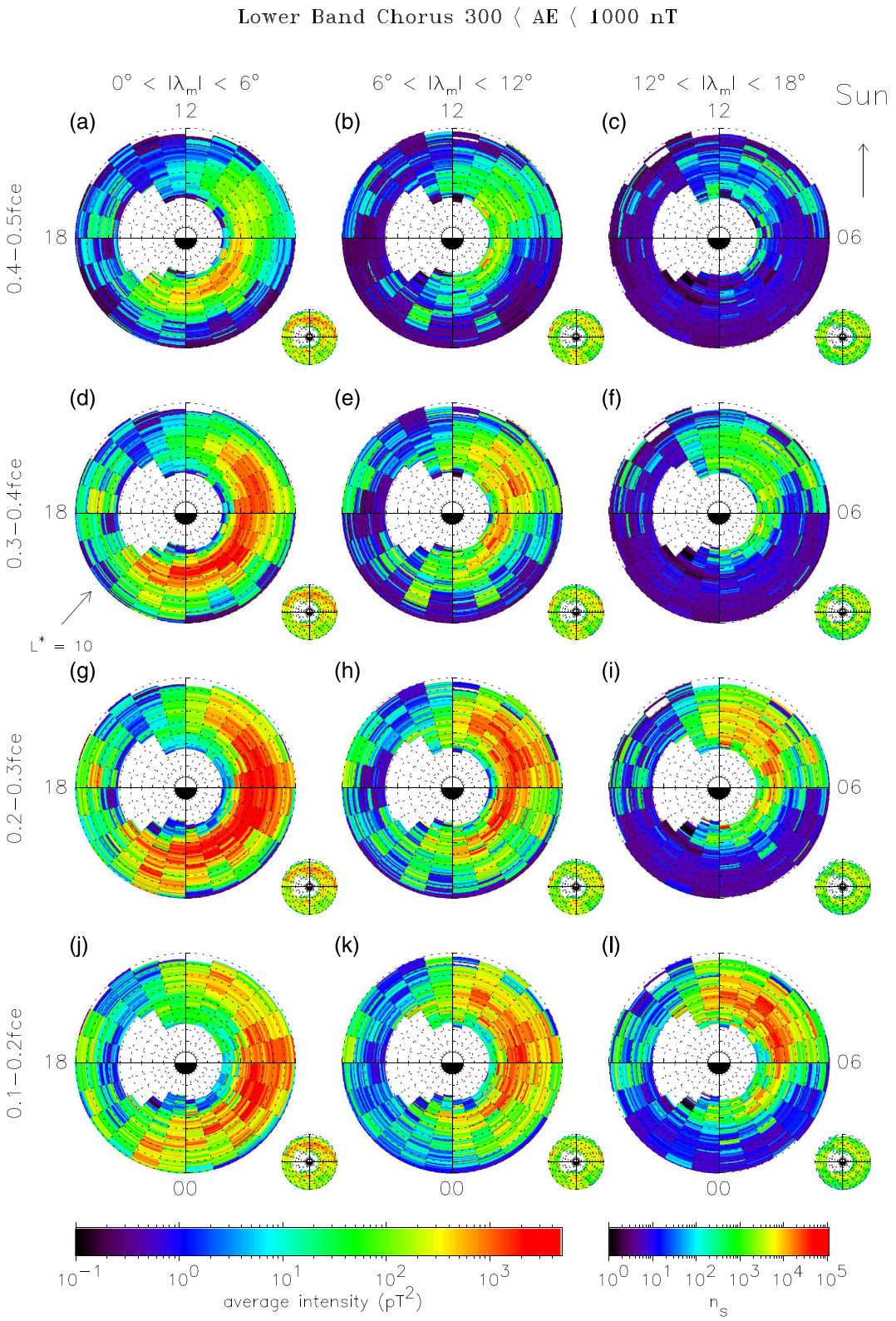

Figure 2. (a–l) Global maps of the average wave intensity of lower-band chorus during active conditions (300 < *AE* < 1,000 nT) as a function of L^* and MLT for, from bottom to top, increasing frequency and, from left to right, increasing magnetic latitude. The maps extend linearly out to $L^* = 10$ with noon at the top and dawn to the right. The average intensities are shown in the large panels and the corresponding sampling distributions in the small panels.

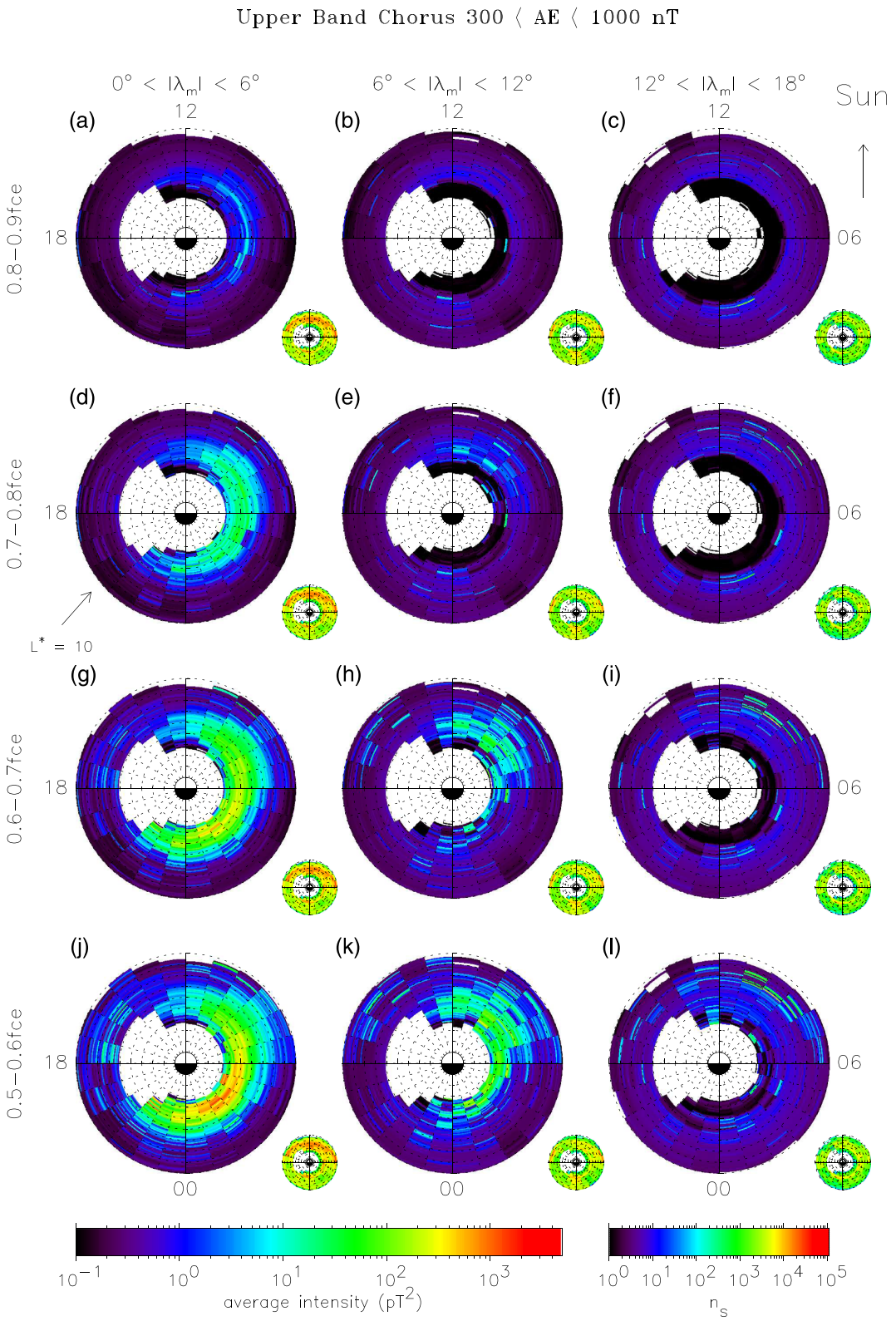

Figure 3. (a–l) Global maps of the average wave intensity of upper-band chorus during active conditions (300 < *AE* < 1,000 nT) as a function of L^* and MLT for, from bottom to top, increasing frequency and, from left to right, increasing magnetic latitude. The maps extend linearly out to $L^* = 10$ with noon at the top and dawn to the right. The average intensities are shown in the large panels, and the corresponding sampling distributions in the small panels.

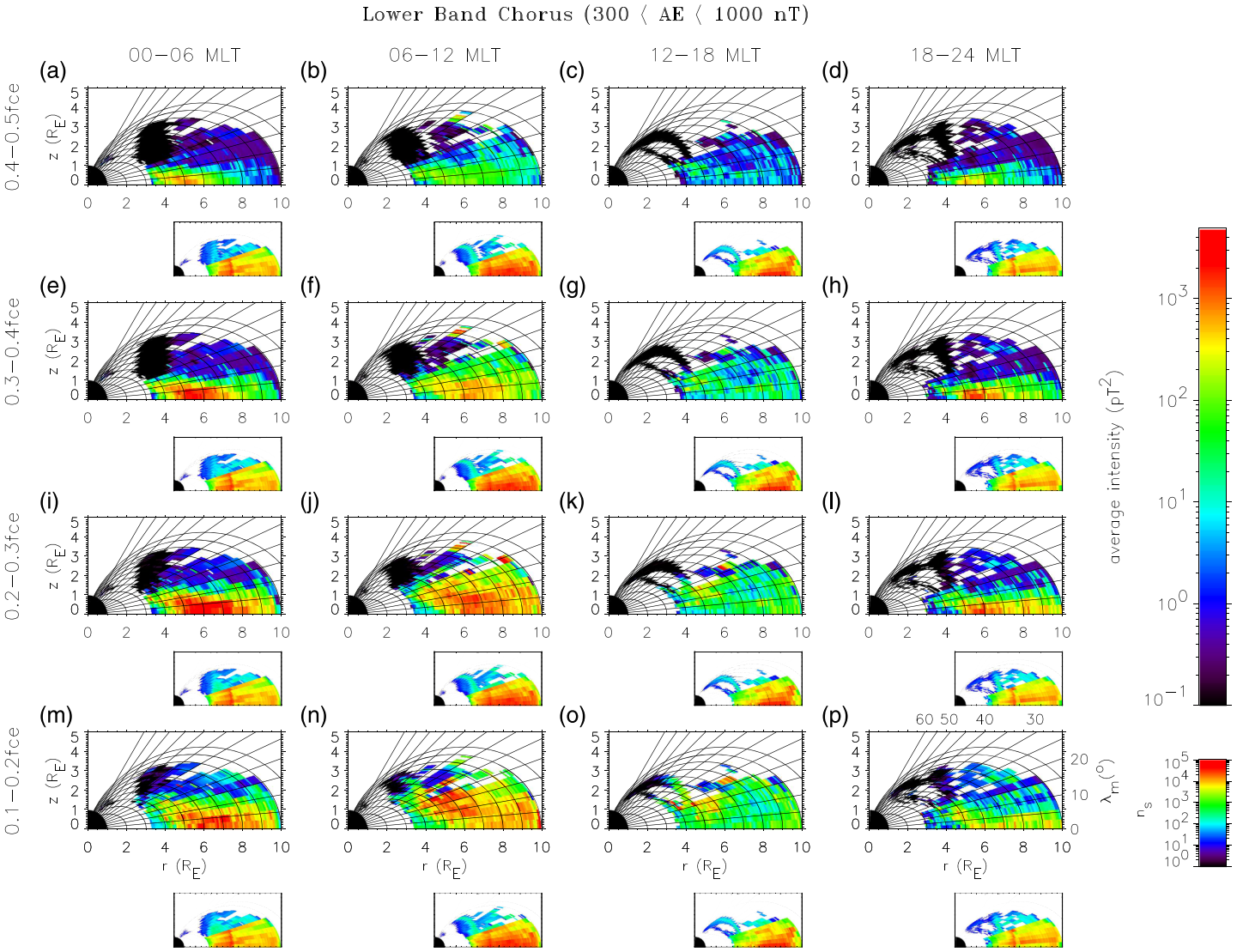

Figure 4. (a–p) Global maps of the average wave intensity of lower-band chorus during active conditions ($300 < AE < 1{,}000$ nT) in the meridional plane for, from bottom to top, increasing frequency and, from left to right, increasing MLT. The average intensities are shown in the large panels, and the corresponding sampling distributions in the small panels.

in contrast to the strong equatorial waves, they do not extend into the premidninght sector and they do not extend beyond $L^* = 6$ in the postmidnight sector. Strong wave power in this region is also seen in the 0.1–0.2f_{ce} (Figure 2k) and 0.3–0.4f_{ce} (Figure 2e) bands, but it is less extensive, as in the equatorial region. In contrast to the equatorial region, strong waves are not observed in the 0.4–0.5f_{ce} band (Figure 2b).

Moving further from the equator, in the region $12 < |\lambda_m| < 18°$, strong waves are restricted to the frequency bands between 0.1 and 0.3f_{ce}. Strong waves in this region cover the largest region of geospace in the 0.1–0.2f_{ce} band. On the dayside strong waves are observed from 06–13 MLT, predominantly in the region $5 < L^* < 7$ (Figure 2l). However, strong waves are largely absent on the nightside. Strong wave power in this region is seen in the 0.2–0.3f_{ce} band (Figure 2i), but it is less extensive. In contrast to the equatorial region, strong waves are not observed in the either the 0.3–0.4f_{ce} or the 0.4–0.5f_{ce} bands (Figures 2f and 2c, respectively).

To investigate the spatial and frequency dependence of upper-band chorus, we plot the average wave intensity during active conditions as a function of L^* and MLT in Figure 3 for, from bottom to top, increasing frequency and, from left to right, increasing magnetic latitude. Here the power is strongest in the 0.5–0.6f_{ce} band in the region $4 < L^* < 5.5$ closest to the equator (Figure 3j). The upper-band chorus does not extend

significantly to higher latitudes and is entirely absent in the region $12 < |\lambda_m| < 18°$. Furthermore, the upper-band chorus is more tightly confined in L^* with little wave power being observed beyond $L^* = 7$.

3.3. Latitudinal Distribution

To investigate the latitudinal distribution of lower-band chorus in more detail, we plot the average wave intensities in the meridional plane in Figure 4 for, from bottom to top, increasing frequency and, from left to right, increasing MLT. Dipole field lines and lines of constant magnetic latitude are included to help visualize the behavior of the wave intensities as a function of L^* and $|\lambda_m|$. The average intensities are shown in the large panels, and the corresponding sampling distributions in the small panels. We include the wave data beyond $\lambda_m = 18°$ for illustrative purposes, but note that the coverage is much reduced at the higher latitudes. On the nightside the strongest wave power tends to be confined to within 6° of the geomagnetic equator, with the exception of the region $4 < L^* < 6$ where the stronger wave power can extend to higher latitudes, around 12°, in the postmidnight sector (Figures 4e, 4i, and 4m). The strongest waves extend to higher latitudes in the prenoon sector, where large intensities are observed up to 18° in the region $5 < L^* < 8$ (Figure 4n). The maximum radial extent of the strongest waves decreases with increasing frequency typically ranging from $L^* = 10$ in the 0.1–0.2 (Figures 4m and 4n) and 0.2–0.3f_{ce} bands (Figures 4i and 4j), $L^* = 8$ in the 0.3–0.4f_{ce} band (Figures 4e and 4f), and $L^* = 6$ in the 0.4–0.5f_{ce} band (Figure 4a).

4. Discussion

The chorus source region is located close to the geomagnetic equatorial plane (LeDocq et al., 1998; Santolík & Gurnett, 2003; Santolík et al., 2005). For example, Lauben et al. (2002) found that the source region is typically located within about 5° of the magnetic equatorial plane. The global distribution of chorus in the equatorial region, $|\lambda_m| < 6°$, thus corresponds to the distribution of the waves in the source region. This is where the waves are generated and analysis of these global maps essentially reveals where the chorus is generated as a function of L^*, MLT and normalized frequency.

Our results show that the global distribution of the chorus wave power in the equatorial source region depends strongly on normalized frequency. Since chorus is generated by anisotropic electron distributions, the observed distribution of the chorus wave power in this region is likely to be strongly related to the distributions and anisotropies of the resonant electrons. If we assume that the ratio of the electron plasma frequency to the electron gyrofrequency, f_{pe}/f_{ce}, is 4 in the trough region outside of the plasmapause (see, e.g., Lam et al., 2010), then the electron minimum resonant energies for interaction with parallel propagating whistler mode waves will typically be in the range of 10–40 keV for waves with frequencies between 0.2 and 0.4f_{ce}, 4–8 keV in the 0.4–0.5f_{ce} band, and 2–4 keV in the 0.5–0.6f_{ce} band. Large fluxes of 10–30 keV electrons combined with large anisotropies are typically observed inside $L = 8$ near midnight and extend out to larger L values in the prenoon sector (Li et al., 2010), broadly consistent with the region of enhanced chorus wave power in the 0.2–0.4f_{ce} frequency bands. At lower energies (2–10 keV) the flux decreases from midnight through dawn to noon (Li et al., 2010), confining the strong waves in the 0.4–0.5 and 0.5–0.6 f_{ce} bands to postmidnight sector. Here the electron anisotropies maximize inside $L = 6.5$ (Li et al., 2010) and are broadly consistent with the region of enhanced wave power at frequencies between 0.4 and 0.6f_{ce}.

We note that the original wave data that is used to determine the average power in the 0.4–0.5 and 0.5–0.6f_{ce} frequency bands may contain a minimum in the wave power spectral density associated with the well-known gap that can separate lower-band from upper-band chorus (Koons & Roeder, 1990; Tsurutani & Smith, 1977). However, the gap near 0.5f_{ce} is not an omnipresent feature and, when present, varies in central frequency and bandwidth. Teng et al. (2019) studied over 22,000 whistler mode wave events using Van Allen Probes data and found that ~53% were lower-band chorus only, ~8% were upper-band chorus only, ~6% had no gap, and ~17% had a gap. Furthermore, from a statistical study of 7 years of waveform data from the three inner THEMIS probes, Gao et al. (2019) showed that, for times when chorus was present in both the lower and upper bands, about two thirds of the events had a power gap, while a third of the events had no significant power gap. For the events with power gaps, the central frequency of the power gap had a broad distribution ranging from 0.36 to 0.7f_{ce}, peaking at ~0.49f_{ce}. The frequency bandwidth of the power gap also covered a wide frequency range (from 0 to 0.3f_{ce}), peaking at the frequency of ~0.07f_{ce}. In our study the two frequency bands on either side of 0.5f_{ce} are most likely to be affected by the power gap minimum. However, these bands may still both contain significant power due to the fact that the gap is not an omnipresent feature and, when present, due to the variability of the gap position and width.

Moving away from the equatorial source region the global distribution of chorus wave power during active conditions changes dramatically as a function of normalized frequency, L^* and MLT. On the nightside strong chorus waves are tightly confined to the near-equatorial region, being largely restricted to latitudes below 6°. The exception is in the postmidnight sector at low L^* ($L^* < 6$) where strong waves below $0.4f_{ce}$ are also observed at higher latitudes, up to ~12°. In contrast, on the dayside strong lower-band chorus is also observed at higher latitudes, principally in the prenoon sector. Here, there is a clear frequency dependence with strong chorus power observed at frequencies below $0.3f_{ce}$ but not above. We suggest that the behavior of the chorus wave power outside of the generation region is dominated by Landau damping by suprathermal electrons which is known to be more efficient at higher frequencies and larger values of L^* and less efficient in the prenoon sector (Bortnik et al., 2007).

The chorus wave power is generally strongest at the equator. However, the prenoon sector at low L^* ($4< L^* <5$) is a notable exception. Here the wave power increases with increasing latitude. This is most likely due to a reduction in the flux of source electrons in this region (Bortnik et al., 2007; Meredith et al., 2011) and relatively low inhomogeneity in the ambient magnetic field, meaning that chorus waves have to travel further along the field line to achieve the threshold level required for nonlinear growth (Bortnik et al., 2007). They are able to do this in the prenoon sector due to the reduction in Landau damping and reduced inhomogeneity (Zhou et al., 2015) as the waves move away from the equatorial region (Bortnik et al., 2007).

Lam et al. (2010) showed that, inside $L = 7$, the global distribution of the precipitating flux of $E > 30$ keV electrons is well correlated with the global distribution of lower-band chorus waves as observed by the CRRES satellite. The global model presented here extends the coverage to $L^* = 10$. During active periods following the passage of a high speed solar wind stream, large fluxes of precipitating $E > 30$ keV electrons are observed from 21 through dawn to 11 MLT, with confinement to lower L shells on the nightside and extending to higher L shells on the dayside (Meredith et al., 2011). This is similar to the spatial extent of the strong wave power observed in the equatorial region in the $0.2–0.3f_{ce}$ frequency band, suggesting that these waves are responsible for the precipitation beyond $L = 7$.

We now have excellent coverage of whistler mode chorus in the $0.1–1.0f_{ce}$ range in the near-equatorial region ($|\lambda_m| < 18°$). However, the coverage is much less extensive at higher latitudes and lower relative frequencies. Results suggest that lower-band chorus can be strong on the dayside in the region $15 < |\lambda_m| < 30°$ (Meredith et al., 2012) and that low frequency chorus, $f_{lhr} < f < 0.1f_{ce}$, where f_{lhr} is the lower hybrid resonance frequency, can be strong on the dayside in the midlatitude region, $15 < |\lambda_m| < 45°$ (Meredith et al., 2014). In pursuit of a complete and fully global set of observations of chorus in the Earth's inner magnetosphere, we require more information at frequencies in the range $f_{lhr} < f < 0.1f_{ce}$ and more data from the midlatitude region, specifically $18 < |\lambda_m| < 45°$.

5. Conclusions

We have extended our database of whistler mode chorus by including ~3 years of plasma wave data from RBSP-A and RBSP-B and an additional ~6 years of data from THEMIS-A, THEMIS-D, and THEMIS-E. Our main conclusions are as follows:

(1) The global distribution of strong chorus waves as a function of L^* and MLT, during active conditions, changes dramatically as a function of both normalized frequency and magnetic latitude.
(2) Close to the equator ($|\lambda_m| < 6°$) the global distribution of strong chorus waves during active conditions essentially reveals the chorus source region as a function of L^*, MLT, and normalized frequency. Here strong wave power is most extensive in the $0.1–0.4\,f_{ce}$ bands in the region 21–11 MLT from the plasmapause out to $L^* = 8$ and beyond, especially near dawn. At higher frequencies, in the $0.4–0.6f_{ce}$ frequency bands, strong wave power is more tightly confined, typically being restricted to the postmidnight sector in the region $4 < L^* < 6$.
(3) The global distribution of strong chorus wave power evolves systematically with increasing magnetic latitude, reflecting propagation effects and broadly consistent with Landau damping by suprathermal electrons. In the region $12 < |\lambda_m| < 18°$ strong waves are largely restricted to the $0.1–0.3\,f_{ce}$ bands in the prenoon sector, where they typically extend from $5 < L^* < 8$.

The new global model of whistler mode chorus has greatly improved the coverage and statistics of our existing model in the near-equatorial region. The new model will be incorporated into the British Antarctic

Survey (BAS) radiation belt model (e.g., Glauert et al., 2014) leading to more accurate space weather models and forecasts. The new model will also enable more accurate testing of current theories on the generation and propagation of whistler mode chorus in the near-equatorial region of the inner magnetosphere.

Data Availability Statement

The results and data shown in this paper can be downloaded from the U.K. Polar Data Centre (https://data.bas.ac.uk and https://doi.org/10.5285/2b0afaea-6931-4a7a-b72f-23feeed2d22a).

Acknowledgments
We acknowledge the CDAWeb (https://cdaweb.sci.gsfc.nasa.gov/index.html/) for the provision of the DE-1 wave data. We thank LPCEE laboratory (Orléans, France) for their help in the analysis of this wave data. We thank the STAFF-DWP instrument team for provision of the Double Star TC1 data, which are available at the Cluster Science Archive (https://www.cosmos.esa.int/web/csa). We thank NASA Contract NAS5-02099 and V. Angelopoulos for use of data from THEMIS mission. Specifically, we thank O. Le Contel and A. Roux for use of SCM data, which are available from the website (http://themis.ssl.berkeley.edu/data/themis/). We are grateful for the Van Allen Probes data from the EMFISIS instrument obtained from the website (https://emfisis.physics.uiowa.edu/data/index). We acknowledge the NSSDC Omniweb for the provision of the geomagnetic activity indices used in this report. The research leading to these results has received funding from the Natural Environment Research Council Highlight Topic Grant NE/P10738X/1 (Rad-Sat) and the NERC Grant NE/R016038/1. W. L. and X. S. would like to acknowledge support from NASA Grants NNX17AG07G and 80NSSC19K0845, NSF Grant AGS-1847818, and the Alfred P. Sloan Research Fellowship FG-2018-10936. J. B. would like to acknowledge support from NASA Grants NNX14AI18G, and RBSP-ECT and EMFISIS funding provided by JHU/APL Contracts 967399 and 921647 under NASA's prime contract NAS5-01072.

References

Agapitov, O. V., Mourenas, D., Artemyev, A. V., Mozer, F. S., Hospodarsky, G., Bonnell, J., & Krasnoselskikh, V. (2018). Synthetic empirical chorus wave model from combined Van Allen Probes and Cluster statistics. *Journal of Geophysical Research: Space Physics*, *123*, 297–314. https://doi.org/10.1002/2017JA024843

Bortnik, J., Li, W., Thorne, R. M., Angelopoulos, V., Cully, C., Bonnell, J., Le Contel, O., & Roux, A. (2009). An observation linking the origin of plasmaspheric hiss to discrete chorus emissions. *Science*, *324*(5928), 775–778. https://doi.org/10.1126/science.1171273

Bortnik, J., Thorne, R. M., & Meredith, N. P. (2007). Modeling the propagation characteristics of chorus using CRRES suprathermal electron fluxes. *Journal of Geophysical Research*, *112*, A08204. https://doi.org/10.1029/2006JA012237

Bortnik, J., Thorne, R. M., & Meredith, N. P. (2008). The unexpected origin of plasmaspheric hiss from discrete chorus emissions. *Nature*, *452*, 62–66. https://doi.org/10.1038/nature06741

Gao, X., Chen, L., Li, W., Lu, Q., & Wang, S. (2019). Statistical results of the power gap between lower-band and upper-band chorus waves. *Geophysical Research Letters*, *46*, 4098–4105. https://doi.org/10.1029/2019GL082140

Glauert, S. A., Horne, R. B., & Meredith, N. P. (2014). Three-dimensional electron radiation belt simulations using the BAS radiation belt model with new diffusion models for chorus, plasmaspheric hiss, and lightning-generated whistlers. *Journal of Geophysical Research: Space Physics*, *119*, 268–289. https://doi.org/10.1002/2013JA019281

Hartley, D. P., Kletzing, C. A., Chen, L., Horne, R. B., & Santolík, O. (2019). Van Allen Probes observations of chorus wave vector orientations: Implications for the chorus-to-hiss mechanism. *Geophysical Research Letters*, *46*, 2337–2346. https://doi.org/10.1029/2019GL082111

Horne, R. B., Thorne, R. M., Glauert, S. A., Albert, J. M., Meredith, N. P., & Anderson, R. R. (2005). Timescale for radiation belt electron acceleration by whistler mode chorus waves. *Journal of Geophysical Research*, *110*, A03225. https://doi.org/10.1029/2004JA010811

Koons, H. C., & Roeder, J. L. (1990). A survey of equatorial magnetospheric wave activity between 5 and 8 RE. *Planetary Space Science*, *38*, 1335–1341. https://doi.org/10.1016/0032-0633(90)90136-E

Lam, M. M., Horne, R. B., Meredith, N. P., Glauert, S. A., Moffat-Griffin, T., & Green, J. C. (2010). Origin of energetic electron precipitation >30 keV into the atmosphere. *Journal of Geophysical Research*, *115*, A00F08. https://doi.org/10.1029/2009JA014619

Lauben, D. S., Inan, U. S., Bell, T. F., & Gurnett, D. A. (2002). Source characteristics of ELF/VLF chorus. *Journal of Geophysical Research*, *107*(A12), 1429. https://doi.org/10.1029/2000JA003019

LeDocq, M. J., Gurnett, D. A., & Hospodarsky, G. B. (1998). Chorus source locations from VLF Poynting flux measurements with the Polar spacecraft. *Geophysical Research Letters*, *25*(21), 4063–4066. https://doi.org/10.1029/1998GL900

Li, W.,Thorne, R. M., Nishimura, Y., Bortnik, J., Angelopoulos, V., McFadden, J. P., et al. (2010). THEMIS analysis of observed equatorial electron distributions responsible for the chorus excitation. *Journal of Geophysical Research*, *115*, A00F11. https://doi.org/10.1029/2009JA014845

Li, W., Ma, Q., Thorne, R. M., Bortnik, J., Kletzing, C. A., Kurth, W. S., et al. (2015). Statistical properties of plasmaspheric hiss derived from Van Allen Probes data and their effects on radiation belt electron dynamics. *Journal of Geophysical Research Space Physics*, *120*, 3393–3405. https://doi.org/10.1002/2015JA021048

Li, W., Thorne, R. M., Angelopoulos, V., Bortnik, J., Cully, C. M., Ni, B., et al. (2009). Global distribution of whistler-mode chorus waves observed on the THEMIS spacecraft. *Geophysical Research Letters*, *36*, L09104. https://doi.org/10.1029/2009GL037595

Li, W., Thorne, R. M., Bortnik, J., Tao, X., & Angelopoulos, V. (2012). Characteristics of hiss-like and discrete whistler-mode emissions. *Geophysical Research Letters*, *39*, L18106. https://doi.org/10.1029/2012GL053206

Lorentzen, K. R., Blake, J. B., Inan, U. S., & Bortnik, J. (2001). Observations of relativistic electron microbursts in association with VLF chorus. *Journal of Geophysical Research*, *106*, 6017–6027. https://doi.org/10.1029/2000JA003018

Lyons, L. R., & Thorne, R. M. (1973). Equilibrium structure of radiation belt electrons. *Journal of Geophysical Research*, *78*(13), 2142–2149. https://doi.org/10.1029/JA078i013p02142

Meredith, N. P., Horne, R. B., & Anderson, R. R. (2001). Substorm dependence of chorus amplitudes: Implications for the acceleration of electrons to relativistic energies. *Journal of Geophysical Research*, *106*(A7), 13,165–13,178. https://doi.org/10.1029/2000JA900156

Meredith, N. P., Horne, R. B., Glauert, S. A., & Anderson, R. R. (2007). Slot region electron loss timescales due to plasmaspheric hiss and lightning generated whistlers. *Journal of Geophysical Research*, *112*, A08214. https://doi.org/10.1029/2006JA012413

Meredith, N. P., Horne, R. B., Glauert, S. A., Baker, D. N., Kanekal, S. G., & Albert, J. M.(2009). Relativistic electron loss timescales in the slot region. *Journal of Geophysical Research*, *114*, A03222. https://doi.org/10.1029/2008JA013889

Meredith, N. P., Horne, R. B., Kersten, T., Li, W., Bortnik, J., Sicard, A., & Yearby, K. H. (2018). Global model of plasmaspheric hiss from multiple satellite observations. *Journal of Geophysical Research: Space Physics*, *123*, 4526–4541. https://doi.org/10.1029/2018JA025226

Meredith, N. P., Horne, R. B., Lam, M. M., Denton, M. H., Borovsky, J. E., & Green, J. C. (2011). Energetic electron precipitation during high-speed solar wind stream driven storms. *Journal of Geophysical Research*, *116*, A05223. https://doi.org/10.1029/2010JA016293

Meredith, N. P., Horne, R. B., Li, W., Thorne, R. M., & Sicard-Piet, A. (2014). Global model of low-frequency chorus (fLHR $0.1f_{ce}$) from multiple satellite observations. *Geophysical Research Letters*, *41*, 280–286. https://doi.org/10.1002/2013GL059050

Meredith, N. P., Horne, R. B., Sicard-Piet, A., Boscher, D., Yearby, K. H., Li, W., & Thorne, R. M.(2012). Global model of lower band and upper band chorus from multiple satellite observations. *Journal of Geophysical Research*, *117*, A10225. https://doi.org/10.1029/2012JA017978

Miyoshi, Y., Kataoka, R., Kasahara, Y., Kumamoto, A., Nagai, T., & Thomsen, M. F. (2013). High-speed solar wind with southward interplanetary magnetic field causes relativistic electron flux enhancement of the outer radiation belt via enhanced condition of whistler waves. *Geophysical Research Letters*, *40*, 4520–4525. https://doi.org/10.1002/grl.50916

Miyoshi, Y., Oyama, S., Saito, S., Kurita, S., Fujiwara, H., Kataoka, R., et al. (2015). Energetic electron precipitation associated with pulsating aurora: EISCAT and Van Allen Probe observations. *Journal of Geophysical Research: Space Physics*, *120*, 2754–2766. https://doi.org/10.1002/2014JA020690

Nishimura, Y., Bortnik, J., Li, W., Thorne, R. M., Lyons, L. R., et al. (2010). Identifying the driver of the pulsating aurora. *Science*, *330*, 81–84. https://doi.org/10.1126/science.1193186

Olson, W. P., & Pfitzer, K. (1977). Magnetospheric magnetic field modelling annual scientific report. AFOSR Contract No. F44620-75-c-0033.

Omura, Y., Katoh, Y., & Summers, D. (2008). Theory and simulation of the generation of whistler-mode chorus. *Journal of Geophysical Research*, *113*, A04223. https://doi.org/10.1029/2007JA012622

Santolík, O., & Gurnett, D. A. (2003). Transverse dimensions of chorus in the source region. *Geophysical Research Letters*, *30*(2), 1031. https://doi.org/10.1029/2002GL016178

Santolík, O., Gurnett, D. A., Picket, J. S., Parrot, M., & Cornilleau-Wehrlin, N. (2005). Central position of the source region of storm time chorus. *Planetary Space Science*, *53*, 299–305.

Santolík, O., Gurnett, D. A., Pickett, J. S., Parrot, M., & Cornilleau-Wehrlin, N. (2004). A microscopic and nanoscopic view of storm-time chorus on 31 March 2001. *Geophysical Research Letters*, *31*, L02801. https://doi.org/10.1029/2003GL018757

Teng, S., Tao, X., & Li, W. (2019). Typical characteristics of whistler mode waves categorized by their spectral properties using Van Allen Probes observations. *Geophysical Research Letters*, *46*, 3607–3614. https://doi.org/10.1029/2019GL082161

Thorne, R. M. (2013). Rapid local acceleration of relativistic radiation-belt electrons by magnetospheric chorus. *Nature*, *504*, 411–414. https://doi.org/10.1038/nature12889

Thorne, R. M., Ni, B., Tao, X, Horne, R. B., & Meredith, N. P. (2010). Scattering by chorus waves as the dominant cause of diffuse auroral precipitation. *Nature*, *467*, 943–946. https://doi.org/10.1038/nature09467

Thorne, R. M., O'Brien, T. P., Shprits, Y. Y., Summers, D., & Horne, R. B. (2005). Timescale for MeV electron microburst loss during geomagnetic storms. *Journal of Geophysical Research*, *110*, A09202. https://doi.org/10.1029/2004JA010882

Tsurutani, B. T., & Smith, E. J. (1977). Two types of magnetospheric ELF chorus and their substorm dependencies. *Journal of Geophysical Research*, *82*, 5112–5128. https://doi.org/10.1029/JA082i032p05112

Tu, W., Cunningham, G. S., Chen, Y., Morley, S. K., Reeves, G. D., & Blake, J. B. (2014). Event-specific chorus wave and electron seed population models in DREAM3D using the Van Allen Probes. *Geophysical Research Letters*, *41*, 1359–1366. https://doi.org/10.1002/2013GL058819

Zhou, C., Li, W., Thorne, R. M., Bortnik, J., Ma, Q., An, X., et al. (2015). Excitation of dayside chorus waves due to magnetic field line compression in response to interplanetary shocks. *Journal of Geophysical Research: Space Physics*, *120*, 8327–8338. https://doi.org/10.1002/2015JA021530